

Synthesis pathways to thin films of stable layered nitrides

Andriy Zakutayev^{1*}, Matthew Jankousky², Laszlo Wolf², Yi Feng³, Christopher L. Rom¹, Sage R. Bauers¹, Olaf Borkiewicz⁴, David A. LaVan³, Rebecca W. Smaha¹, Vladan Stevanovic²

¹ National Renewable Energy Laboratory

² Colorado School of Mines

³ National Institute of Standards and Technology

⁴ Argonne National Laboratory

*andriy.zakutayev@nrel.gov

Abstract

One of the grand challenges of materials chemistry is the selective synthesis of metastable materials away from equilibrium. Thin film deposition methods with rapid condensation of vapor precursors can readily synthesize metastable phases, but they often struggle to yield the thermodynamic ground state. How can thermodynamically-stable structures for practical applications be grown using kinetically-limited synthesis methods? Here, we reveal a synthesis pathway to thermodynamically-stable ordered layered ternary nitride materials, and we explain why disordered metastable intermediate phases tend to form in the first place. We show that starting from atomically dispersed vapor precursors leads to a 3D long-range disordered MgMoN₂ thin film polymorph product, with a layered short-range order that has a low-energy transformation barrier to the layered 2D-like stable structure. We extend this synthesis approach to ScTaN₂, MgWN₂ and MgTa₂N₃, opening a door to synthesis of other layered nitride thin films with unique semiconducting and quantum properties.

Introduction

Controlled chemical synthesis of metastable solid-state materials away from thermodynamic equilibrium has been one of the grand challenges of basic energy science,¹ widely studied across the polymeric, metallic, and inorganic materials classes. Famous examples of metastable inorganic materials with amazing properties include diamond, anatase TiO₂, martensitic steels, dolomite mineral, and even chocolate. In this work, we address the reciprocal challenge of applied materials development: how to synthesize thermodynamically-stable structures using kinetically-limited thin film deposition methods that tend to favor metastable material polymorphs? Among nitride thin films, examples of metastable thin film materials used for practical applications include MoN as an electrocatalyst for hydrogen evolution² and NbN in superconducting qubits,³ but the corresponding properties of their ground state structures remain largely unknown. An additional reason to find thin film synthesis pathways to stable materials with layered 2D-like structures is that many of them tend to host unusual semiconductor or quantum properties promising for practical applications.⁴ Among nitrides, examples include high mobility in 2D layered hexagonal boron nitride,⁵ 2D electron gas at GaN/AlGaIn interfaces⁶, diverse properties of nitrogen-containing intermetallic MAX phases,^{7,8} and more.

There are many known nitrides that are thermodynamically stable in layered, 2D-like crystal structures reported in the bulk solid state synthesis literature,⁹ such as ScTa₂N₂,^{10,11} MgTa₂N₃,^{12,13} and BaZrN₂.^{14,15} These layered, 2D-like crystal structures feature alternating sheets of MN_x polyhedra (where *M* is a metal and *x*=4–10), such as octahedra, tetrahedra, square pyramids, trigonal prisms, and so on. These layered materials with two different metal coordination environments, are distinct from atomically layered structures that are derived from 3D wurtzites¹⁶ or 3D rocksalts¹⁷ by cation ordering, or derived from 3D perovskites¹⁸ or 3D fluorites (e.g., bixbyites) by anion ordering.¹⁹ Some of these layered, 2D-like nitride materials are theoretically predicted to have unique properties, such as tunable topological and Dirac semimetal states in MgTa₂N₃ based alloys.^{20,21} Unfortunately, their electrical transport and optoelectronic properties remain experimentally unknown, in part due to difficulty in measuring these properties for polycrystalline powders. Single crystals needed for anisotropic measurements are even more challenging to grow in nitride chemistry. In contrast, physical vapor deposition (sputtering) and other synthesis methods that result in thin film suitable for electrical transport measurements often lead to nitrides in metastable phases, up to the highest possible substrate temperature at which the material can be synthesized. These metastable polymorphs, synthesized by rapid quenching from vapor or plasma to solid phase at a rate of up to 10¹⁰ K s⁻¹,²² tend to have isotropic 3D bonding with very different properties compared to the thermodynamically-stable layered 2D-like structures. For instance, a layered 2D-like ground state of MgWN₂ with W in 6-fold trigonal prismatic coordination is a semiconductor, whereas a 3D polymorph of MgWN₂ with W in 6-fold octahedral coordination is a metal.²³

As an example, consider a family of multivalent ternary nitride materials that combine two metal cations with a nitrogen anion in equal amounts and charge balanced stoichiometry,²⁴ such as ZnZrN₂,²⁵ ZnMoN₂,²⁶ and MgWN₂.²³ These materials are thermodynamically stable in layered 2D-like structures according to theoretical calculations and in some cases bulk solid-state synthesis,^{27,28} and they are most easily described as a mixture of the 3D structure archetypes that embody each layer (Fig. 1). Despite the thermodynamically-stable layered 2D-like “wurtsalt” (wurtzite–rocksalt, or WS; see Fig. 1a) structure of ZnZrN₂ and ZnHfN₂ predicted by several independent theoretical studies,²⁹ thin film synthesis of ZnZrN₂ up to 300 °C results in metastable 3D RS or h-BN crystal structures²⁵, and it decomposes at higher substrate temperatures. Similarly, the Zn₃MoN₄–ZnMoN₂ family crystallizes in a 3D wurtzite structure across the entire chemical composition and substrate temperature range, instead of crystallizing in the thermodynamically-stable layered 2D-like “wurtzeline” (wurtzite–nickeline, or WL; see Fig. 1b) structure at ZnMoN₂ composition.²⁶ Recently, MgWN₂ thin film synthesis on a heated substrate also resulted in two

metastable 3D RS and h-BN structures up to its 600 °C decomposition temperature, whereas the stable layered 2D-like “rockseline” (rocksalt–nickeline, or RL; see Fig. 1c) structure was synthesized by bulk ceramic methods.²³ In all cases, growing these ternary thin films on substrates held at higher temperature to achieve the ground state layered structure was not feasible, likely due to re-evaporation of ZnN_x - and MgN_x -based components caused by their high vapor pressure. Other layered nitrides with 1-1-2 stoichiometry (e.g., $FeWN_2$, $MnMoN_2$,³⁰ $CoMoN_2$;³¹ see Fig. 1c) and 1-2-3 stoichiometry (e.g., $MgTa_2N_3$,¹² $MgNb_2N_3$; see Fig. 1d) have been reported in the RL structure by bulk synthesis but not thin film growth. It remains unclear both i) why thin film synthesis favors metastable 3D structures, and ii) how to reliably achieve nitrides with layered 2D-like structures in film form.

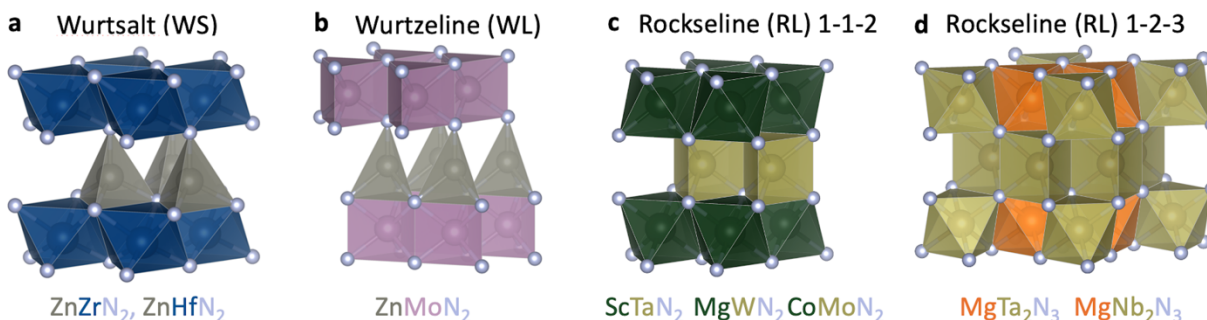


Figure 1: Examples of layered, 2D-like crystal structures among multivalent ternary nitrides: (a) “wurtsalt” wurtzite–rocksalt, or WS, structure consisting of alternating sheets of tetrahedra and octahedra. (b) “wurtzeline” wurtzite–nickeline, or WL, structure consisting of alternating sheets of tetrahedra and trigonal prisms. (c) “rockseline” rocksalt–nickeline, or RL, structure with 1-1-2 stoichiometry consisting of alternating sheets of edge-sharing octahedra and edge-sharing trigonal prisms; and (d) RL structure with 1-2-3 stoichiometry.

From a theoretical point of view, the experimental realizability of various crystalline phases is related to the size of the corresponding local minima on the potential energy surface. The size of a local minimum – the total volume occupied by its attraction basin in the configuration space of atoms – measures the probability to of a structure to fall into that minimum. Hence, a larger basin of attraction implies higher chances for its experimental realization. As was shown previously, this principle explains all experimentally observed metastable polymorphs in several elemental or binary chemistries, such as elemental silicon,³² binary oxides,³³ and group-IV carbides.³⁴ In addition, these arguments based on the size of local minima were successful in explaining the emergence of the disordered RS phase in the thin film synthesis of $ZnZrN_2$ in lieu of the ordered “wurtsalt” ground state.²⁵ However, it is not clear if or how these theoretical methods can explain metastable 3D polymorph formation in other ternary nitride materials or predict transformation pathways to layered 2D-like ground state structures. Answering these questions to integrate such new theoretical methods with experimental synthesis approaches is necessary to accelerate the rate of discovery in inorganic solid-state materials chemistry.

Here we describe a synthesis pathway to nitride thin films with layered 2D-like crystal structures starting from a 3D isotropic precursor, using the multivalent ternary nitride $MgMoN_2$ as an example. While growth on heated substrates results in decomposition above 600 °C, the stable layered 2D-like cation-ordered RL structure of $MgMoN_2$ thin films forms after a relatively mild (700 °C – 1100 °C) post-synthetic heating of the 3D RS precursor deposited at ambient temperature. The emergence of this cation-ordered layered 2D-like product may seem surprising because the 3D isotropic RS structure is an ostensibly cation-disordered sputtered precursor according to X-ray diffraction (XRD), despite the difference in Mg and Mo atom properties. In addition, it shows an unusual negative thermal expansion in the 300 °C – 600 °C range.

Experimental and theoretical pair distribution function (PDF) analysis reveals a layered short-range order in the RS structure, that is reminiscent of the polyhedral layering within the RL structure, which is the key to the emergence of this layered 2D-like product. We theoretically discover a simple displacive transformation pathway from a 3D RS precursor to a layered 2D-like RL product using nudged elastic band calculations, and experimentally quantify a 100 meV/atom transformation barrier using nanocalorimetry measurements. These MgMoN_2 results give a new mechanistic insight into the transformation pathway from 3D precursors to layered 2D-like products, and are extended here to ScTaN_2 , MgWN_2 and MgTa_2N_3 . The discovery of this synthesis pathway opens a door to the synthesis of many other layered materials in thin film form, suitable for quantum property studies using electrical transport measurements.

Results and Discussion

Experimental discovery of rocksalt-to-rockslane phase transformation

We synthesized thin films of Mg–Mo–N by radio-frequency (RF) co-sputtering from metallic Mg and Mo precursors in Ar and N_2 atmosphere, and subjected them to rapid thermal annealing under atmospheric N_2 pressure. The results of composition measurements indicate that the synthesized MgMoN_2 materials in the $\text{Mg}/(\text{Mg}+\text{Mo}) = 0.50 - 0.75$ range (as measured by XRF) are free of oxygen impurities (Fig. 2a, Fig. S1a). According to lab XRD, the as-deposited Mg–Mo–N films form in a nanocrystalline RS-derived crystal structure with mixed Mg and Mo occupancy of the cation lattice across a broad range of studied compositions ($\text{Mg}/(\text{Mg}+\text{Mo}) = 0.20 - 0.95$) and temperatures (Fig. 2b). LeBail fits of the RS lattice constants as a function of cation composition in the as-deposited samples measured by synchrotron grazing incidence XRD at APS show the expected linear trend (Fig. 2c).

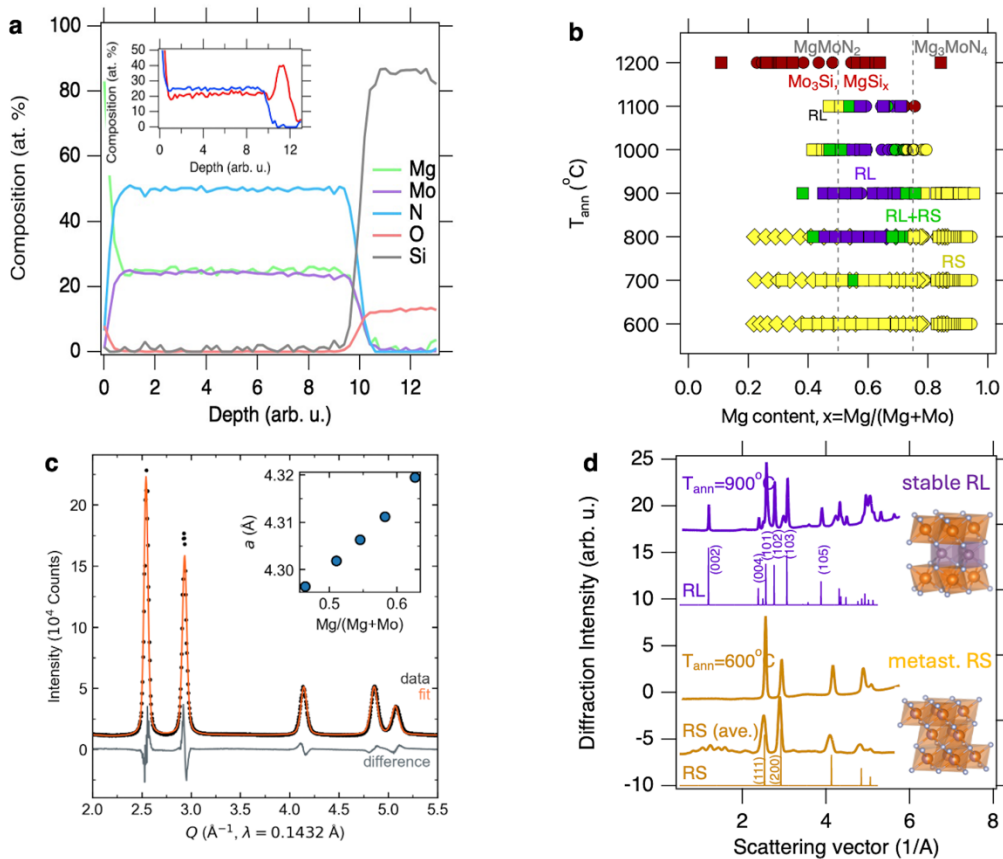


Figure 2: Chemical composition and crystal structure of MgMoN₂: (a) Composition measurements as a function of depth showing negligible amount of oxygen and some Mg accumulation at the substrate interface (inset). (b) Growth map showing formation of the layered 2D-like RL phase at MgMoN₂ and Mg-rich compositions above 700 °C, for several sample libraries indicated by different symbol shapes. (c) LeBail fit performed on synchrotron grazing incidence XRD from APS in the RS structure (s.g.225, *Fm-3m*) for as-deposited films, and the relationship between lattice parameter *a* and cation ratio (inset). (d) Synchrotron GIWAXS data from SSRL and crystal structures of MgMoN₂ in metastable 3D RS and stable layered 2D-like RL phases, along with theoretical reference patterns from ICSD and computationally simulated average disordered RS pattern

After annealing for only 3 min at 700 °C and above, the crystal structure transforms from RS to RL (see Fig. 2c and Fig. 2d), with phase-pure RL material obtained in the Mg/(Mg+Mo) = 0.45 – 0.70 and $T_{\text{ann}} = 800 - 1100$ °C range. We would like to reemphasize that this layered phase cannot be achieved by depositing on the substrate heated to > 700 – 800 °C under low sputtering pressure because even at 600 – 700 °C, there is very little Mg incorporation in the growing film due to high MgN_x vapor pressure (Fig. S2a), similar to MgWN₂²³ and ZnN_x in ZnZrN₂.²⁵ Outside of the Mg/(Mg+Mo) = 0.45 – 0.70 composition window, the RS structure persists after annealing. However, when annealing above 1100 °C (Fig. 2b) and for longer than 3 min (Fig. S1b) a significant reaction of Mo with the Si substrate is observed, as indicated by Mo₃Si diffraction peaks.

The results of synchrotron grazing incidence wide-angle X-ray scattering (GIWAXS) measurements at SSRL for MgMoN₂ films annealed at 600 °C (RS phase) and 900 °C (RL phase) are shown in Fig. 2d alongside the two crystal structure models. All the RS and RL peaks expected from reference patterns are clearly resolved, with some deviation in the peak intensity due to preferential orientation effects or Mg/Mo cation disorder across *O_h*/*T_p* sites. GIWAXS patterns for the Mg₃MoN₄ composition with the RS structure are shown in Fig. S2b. It is peculiar that the measured RL MgMoN₂ data show a strong low-angle (002) and subsequent (00*L*) peaks indicative of some degree of Mg and Mo ordering on the *O_h* and *T_p* sites in the RL structure, whereas the measured RS MgMoN₂ data do not show any peaks related to this long-range cation ordering. This difference poses interesting questions: how does the ostensibly cation-disordered RS structure transition into a clearly cation-ordered RL structure during the annealing process? why does the metastable 3D RS structure form in the first place instead of the stable layered 2D-like RL structure?

Theoretical explanation of metastable rocksalt synthesis

To elucidate the experimental observations described above, we investigated relevant features of the potential energy surface (PES) of MgMoN₂ using the first-principles structure sampling.³³ This method involves generating a large number random structures, relaxing them to the closest local minimum on the potential energy surface, and classifying them into groups of structures with the same underlying structure-type (see Methods). Fig. 3a shows the space group-resolved thermodynamic density of states (TDOS) obtained in the random sampling of 5,000 structures for the structure types that contain 10 or more members. The energy spread of each structure type is due to the variations in the Mg/Mo site occupancies. The tallest peak in the TDOS with 314 members has the RS-type parent structure (s.g.225), with the relatively narrow energy range of 0.5 – 1.5 eV/f.u. This result is consistent with the observation that the RS structure seems able to accommodate cation disorder without large energy differences between different configurations in entropy-stabilized ceramics. The TDOS plot also shows that there are two other relatively populous 6-fold coordinated hexagonal structures (s.g.160 and s.g.166) with 10x – 50x smaller representation than RS, made of edge- and face-sharing octahedra (s.g.166) or a combination of octahedra and trigonal prisms (s.g.160) which can be viewed as a disordered version of the ground state s.g.194 (shown as a dashed line in Fig. 3a). The low symmetry structure-types (s.g.1 and s.g.2) have

high energy and large spread, so they do not contribute to configurational thermodynamics, but instead are important for description of the amorphous/glassy state.³⁵

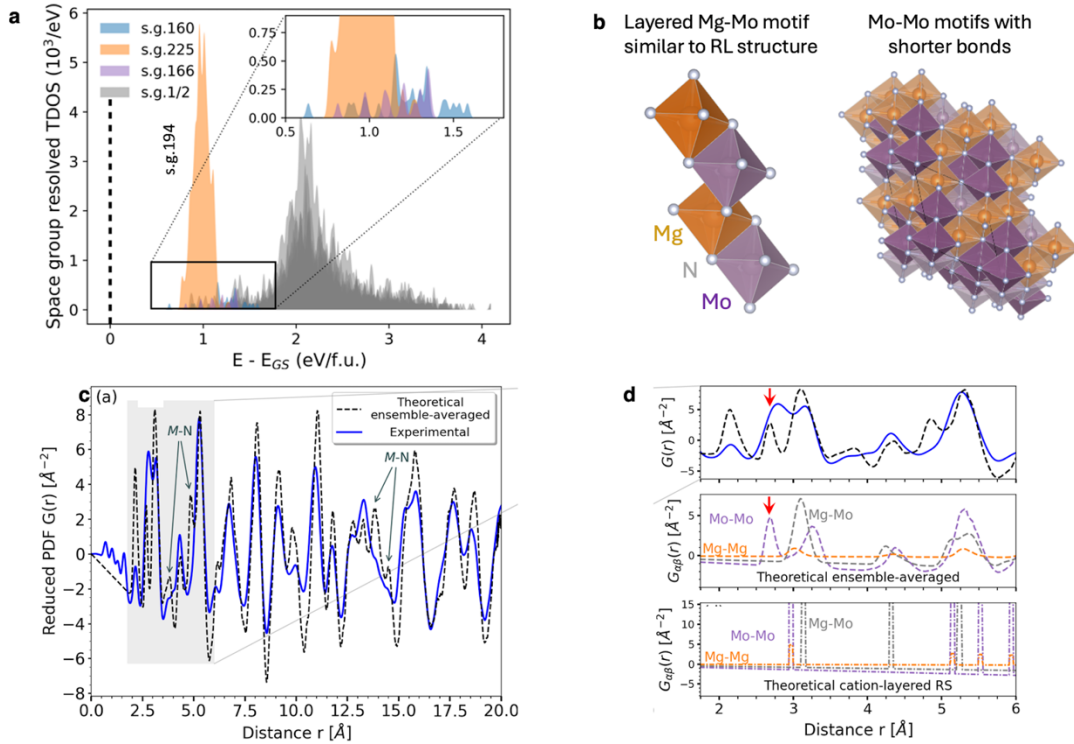


Figure 3: Local short-range atomic order in metastable RS MgMoN₂ (a) Space group-resolved thermodynamic density of states (TDOS) of MgMoN₂ obtained using first-principles random structure sampling. (b) The cation-layered -Mg-Mo-Mg-Mo RS motif along (111) axis (left), taken from a RS structure predicted by structure sampling (right), with shortened Mo–Mo distances (2.62 Å, 2.75 Å, 2.72 Å) in the highlighted MoN₆ octahedra. (c) Reduced PDF $G(r)$ of as-deposited MgMoN₂ data (blue line) and theoretical model from structure sampling (dashed black line). (d) Magnified comparison of theoretical and experimental PDF in the low- r region, with a red arrow indicating the 2.7 Å peak that does not exist in the cation-disordered RS model but results from Mo–Mo interactions (top); M – M partial PDFs that compose the theoretical curve from (middle); and M – M partial PDFs obtained for the cation-layered RS motif (bottom).

Fig. S3a displays the temperature dependence of the configurational free energies of all structure-types from the structure sampling.²⁷ Our calculations include the RL phase, which is represented by the dashed line and assumed to have no configurational entropy (occurrence of 1). The RS phase of MgMoN₂ has the highest entropy because of its large and narrow TDOS, and it becomes the lowest free energy structure for temperatures above 2000 K (Fig. S3b). The as-deposited films at ambient conditions exhibit a cation-disordered RS structure predicted above 2000 K because their kinetically-frozen cation disorder corresponds to this effective temperature. It has been shown that equilibrium calculations for 1000 K – 2500 K temperatures reproduce the cation disorder that exists in materials grown in thin-film form at non-equilibrium conditions, such as ZnZrN₂,²⁵ Co₂ZnO₄, and Co₂NiO₄.³⁶

Interestingly, the RL phase known from bulk synthesis of MgMoN₂ (s.g.194)^{27,28} did not occur a single time in the random structure sampling, indicating that the stable layered RL structure of MgMoN₂ has a very

narrow local minimum on the PES. This is a markedly different result than for ZnZrN_2 and for all other systems we investigated, for which the ground state structures are consistently found by the structure sampling. However, atomic motifs having a -Mg-Mo-Mg-Mo- cation ordering, referred to as the “cation-layered RS motif,” were successfully identified within all RS-type structures from the structure sampling (Fig. 3b). In these motifs, Mo(1) is in the [110] crystallographic direction from Mg(1), Mg(2) is in the [101] direction from Mo(1), and Mo(2) is in the [110] crystallographic direction from Mg(2). Periodic boundary conditions applied to this motif result in the (111) superlattice with alternating Mg and Mo layers.

This four-atom -Mg-Mo-Mg-Mo- motif would be statistically probable to find even in a fully random alloy because the probability of finding a single sequence of four atoms occupied in a certain way is $(1/2)^4$. Moreover, given the relatively large number of ways a given motif can be constructed, a large fraction of cations can be expected to be a part of at least one such motif. It is then not a surprise that the motif is omnipresent - it is found in every random structure in our calculations. Therefore, we hypothesize that the long-range ordered RL phase is experimentally realized (Fig. 2) by a facile structural transformation from the short-range ordered RS phase (Fig. 3b). For this to happen at the relatively low annealing temperature of 700 °C, the experimental RS precursor should contain domains where the local arrangement of Mg and Mo atoms provides a seed for alternating (111) layers, similar to the alternating (001) planes of the RL product.

Comparison of the local structure from theoretical and experimental PDF

The short-range cation order in the long-range disordered RS precursors was measured using synchrotron grazing incidence PDF at APS on a series of pre-annealed thicker (600 – 800 nm) MgMoN_2 samples, with the quartz substrate contribution measured and subtracted. The results of composition-dependent XRD measurements and LeBail fits (Fig. S4b) are consistent with the lattice constant linearly increasing as a function of Mg composition (Fig. 2c). The measured PDF was fit using a randomly disordered RS model across a wide r -range (2 – 30 Å, see Fig. S4a). While the high- r range (> 10 Å) matched this model well, a surprising difference is the short-distance local ordering range (2 – 7 Å) where the PDF fit residuals are high, especially in the 2.5 – 3.0 Å region. This implies that the length scale of the short-range correlations is on the order of 5 Å, that would be hidden from traditional long-range XRD measurements. The lowest- r (< 2 Å) oscillations of the experimental data are due to truncated Fourier transform effects and substrate correction.

To understand the difference(s) between the experimentally measured PDF and the disordered rocksalt PDF model in the 2.0 – 3.0 Å region, a theoretical PDF was obtained through ensemble averaging over all RS-type structures (Fig. 3a), as shown in Fig. 3c. The positions of peaks in the experimental data are well matched by the theoretical model across the entire r -region, including the 2 – 3 Å range (Fig. 3d, top panel) where the random cation disordered RS model fails (Fig. S4a).

Fig. 3d shows the contributions of specific atom type pairs to the PDF (denoted as the partial PDF) in the local structure region for the ensemble-averaged theoretical PDF (middle panel), and the PDF of the cation-layered RS motif (bottom panel), respectively. In the cation-layered RS motif the nearest-neighbor Mo–Mo and Mg–Mg partial peaks are superimposed at the same distance $r = 3.1$ Å (Fig. 3, bottom). In the ensemble-averaged theoretical PDF of the disordered RS model (Fig. 3d, middle), the Mg–Mo and the Mg–Mg partial peaks are present at similar distances ($r = 2.95$ Å), but the Mo–Mo partial is split into two peaks: a peak blending with the Mg–Mo peak at $r = 3.2$ Å, and most importantly another peak around $r = 2.7$ Å where no other partial PDF has a contribution. We identify that this splitting arises from the relaxations of the Mo atoms towards shorter distances that occur in disordered RS-type structures (Fig. 3d, middle).

The isolated shorter distance Mo–Mo peak at 2.7 Å is also known in other layered ternary transition metal nitrides.¹⁰ This modeled Mo–Mo peak explains the measured PDF peak at approximately $r = 2.0 - 3.0$ Å (see Fig. 3d, top) that is not captured by fits to a cation-disordered RS model (see Fig. S4a). It is unlikely that this measured peak is due to Mo–Mo distances in the metallic bcc-Mo structure, because its intensity scales with Mg content (Fig. S4b) and because the single-phase RS XRD LeBail fit residuals are low (Fig. S3b). The overall agreement between experimental and theoretical PDFs (Fig. 3c), and especially the agreement for the distinct Mo-Mo peak in 2.5-3.0 Å range, are the evidence for the similarity between the as-grown MgMoN₂ thin films and the ensemble average of RS-type structure samples (Fig. 3a), but not the RS model with random cation disorder (Fig. S4a). Due to this direct correspondence, the cation-layered -Mg-Mo-Mg- motif found in the RS-type samples structures (Fig. 3b), is theorized to also be found in the as-grown MgMoN₂ thin films. For this cation-layered RS motif (Fig. 3b), to transform to the site-layered RL structure, the kinetic barrier between these two phases should be low, as addressed next.

Measurements and calculations of the transformation pathway

To characterize the RS-to-RL crystallographic transformation process, we performed temperature-dependent laboratory XRD measurements on select samples at the MgMoN₂ composition. The XRD color intensity map as a function of measurement temperature (Fig. 4a) shows a sharp transition around 700 – 720 °C where RL peaks appear and RS peaks disappear, suggesting a facile transformation pathway between the two. It is also interesting to note the unusual negative thermal expansion of the RS lattice in the 300 – 600 °C range (Fig. S5). Time-dependent laboratory XRD measurements at two different temperatures in this range show a gradual increase of the RS (111) peak intensity and decrease of the RL (012) peak intensity on the scale of 30 – 60 minutes (Fig. S6). Fitting the XRD data measured at 700 °C and 712 °C to a sigmoidal Avrami equation from the Johnson–Mehl–Avrami–Kolmogorov (JMAK) model³⁷ in both cases leads to an exponent value of approximately $n = 1.7$ (Fig. 4b). Given the characteristically sharp temperature dependence (Fig. 4a), we assume an instantaneous heterogeneous nucleation process ($n_n = 0$). The measured $n = 1.7$ exponent could correspond to a combination of 2D interface-controlled growth ($n_g = 2$) that could be rationalized by the 2D thin film geometry, and a 3D diffusion-controlled growth ($n_g = 1.5$) that could be rationalized by the observation of the long-range Mg–Mo atom diffusion (Fig. 2a)

To measure the energy scale of the phase transformation process, we performed nanocalorimetry measurements in UHP N₂³⁸ for 100 nm thin MgMoN₂ films deposited on microfabricated Si chips. The apparent heat capacity as a function of measurement temperature (Fig. 4c) shows an endothermic signal that is 25 °C in width and approximately 10 kJ/mol (100 meV/at) in the integrated energy value. It is not entirely clear why this endotherm appears at 550 – 600 °C instead of at 700 °C, the temperature at which the phase transformation is observed by both ex-situ XRD (Fig. 2) and in-situ XRD (Fig. 4a), with possible temperature measurement error accounting for 25 – 75 °C. Possible physical reasons include (a) the need for growth of the locally transformed nuclei to be observed by extended crystal structure measurement methods, and (b) strong dependence of the phase transformation process on the heating rate (0.1 – 10 K/s for XRD vs. 10³ – 10⁴ K/s for nanocalorimetry). Nevertheless, the precise measurement of the small 100 meV/at calorimetry signal for a 100 nm nitride thin film is quite unique, and it is indicative of a relatively low kinetic barrier of the phase transformation process.

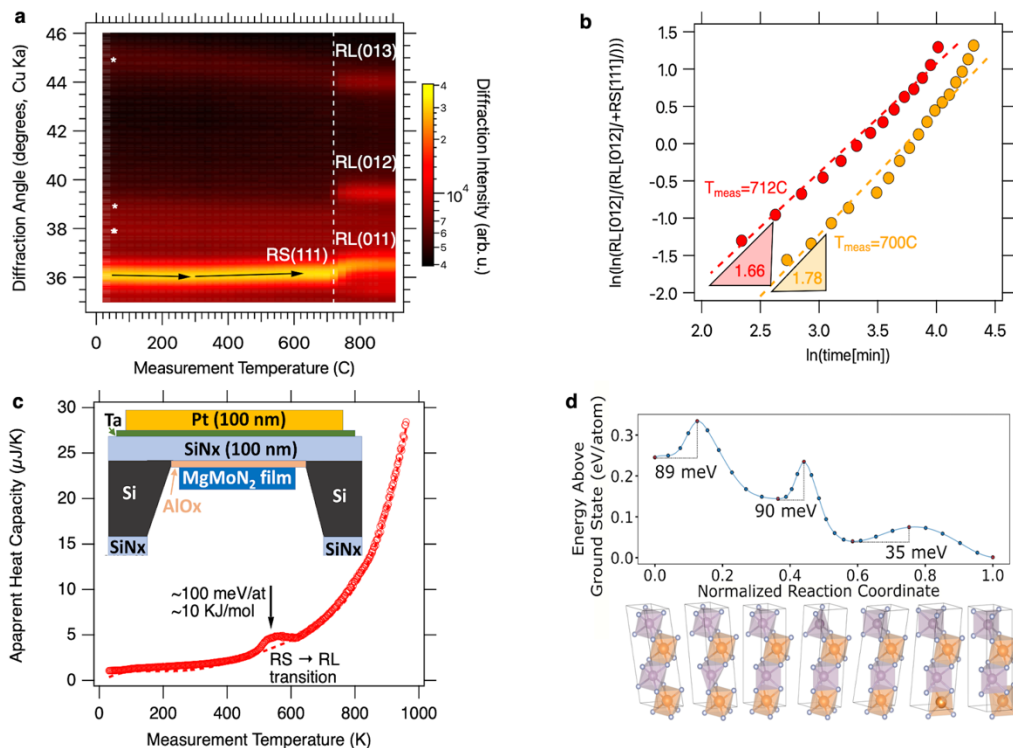


Figure 4: In-situ measurements of the MgMoN_2 RS-RL phase transformation. (a) Temperature-dependent XRD showing negative thermal expansion of RS phase in the 300 °C – 600 °C range and a sharp transition to RL phase around 700 °C. Asterisks indicate broad peaks from a polymeric sample cover dome. (b) Analysis of these time-dependent measurements at 700 °C and 712 °C, resulting in a slope of $n=1.7$, which reflects the combination of instantaneous 2D nucleation ($n=1.5$) and 3D diffusion ($n=2.0$). (c) Nanocalorimetry measurement results, showing a small endothermic signal associated with overcoming the RS-RL energy barrier, using measurement chip (inset). (d) The energy profile and the corresponding structure of the transformation of the layered RS structure to the RL structure as calculated using SS-NEB.

To calculate the energy barrier, we modeled the transformation pathway from the cation-disordered 3D RS phase to the cation-ordered 2D-like RL structure.³⁹ We identified a transformation pathway from an ordered RS structure ($\alpha\text{-NaFeO}_2$ -type) to the ordered RL structure with a relatively low barrier of approximately 90 meV/atom, shown in blue in Fig. 4d. This calculated barrier agrees with the experimental observation that the transition occurs at approximately 600 – 700 °C, and it is also consistent with the apparent change in heat capacity during that transition. The agreement between the calculated barrier and the experimental transition temperature and change in heat capacity supports the hypothesis that small domains of the cation-layered RS motif are present in the experimentally grown thin film. The first step of this pathway involves the transformation of layers of MoN_6 octahedra to MoN_6 trigonal prisms and is characterized by the relative shift of a layer of N atoms: one Mo–N bond per Mo atom is broken and then reformed in this process (90 meV/atom). In the second step, the layers of MgN_6 octahedra must invert: one Mg atom per two formula units must move, and the movement of Mg atoms occurs in every other layer, with two Mg–N bonds per Mg atom are broken (35 meV/atom). The barrier is not expected to change significantly with the introduction of cation disorder to the material, as shown for the barriers in supercells with Mg and Mo sites swapped (Fig. S7), though the 90 meV/atom rate limiting step switched from first to the second one.

Discussion of RL MgMoN₂ crystallization mechanisms

In this work, we experimentally discovered (Figs. 2, 4) and theoretically explained (Figs. 3, 4) a synthesis pathway to nitride thin films with layered 2D-like crystal structures (Fig. 1) from 3D atomically mixed precursors. The key new insights are that:

- (i) The 3D structures are high-probability metastable phases favored by kinetically limited growth methods (Fig. 2, 3), whereas stable 2D-layered structures have low probability of formation.
- (ii) A layered 2D-like crystal structure can form by facile atomic transformation (Fig. 4) from a 3D precursor that has no long-range cation order but features layered cation-ordered local motifs (Fig. 3).
- (iii) These motifs (Fig. 3) serve as nucleation centers for this crystallographic transformation into a long-range ordered 2D-like structure experimentally achieved by annealing (Fig. 2, 4).

This new synthetic pathway is supported by direct comparison of measured and calculated PDF (Fig. 3) and the energy barrier (Fig. 4) between the 3D precursor and the 2D-like product.

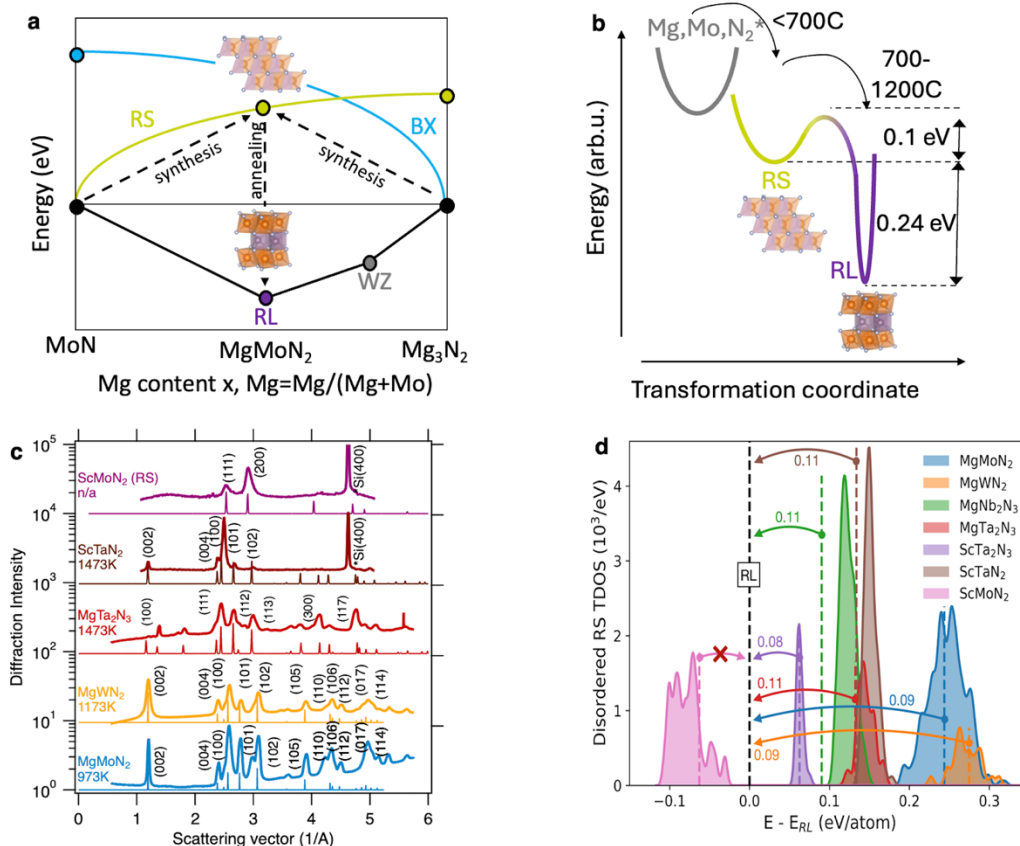


Figure 5: 3D-to-2D synthesis pathway for MgMoN₂ and extension to other materials chemistries: (a) Convex hull diagram, showing co-deposition of a high-energy 3D RS MgMoN₂ precursor and its crystallographic transformation to the layered 2D-like RL product, with BX indicating the competing bixbyite structure of Mg₃N₂. (b) Potential energy landscape at a fixed MgMoN₂ composition, showing a low-energy 0.1 eV barrier between the broad metastable 3D RS energy valley and a stable deep, narrow 2D-like RL energy well. (c) Experimentally-measured synchrotron GIWAXS patterns of four new layered 2D-like RL thin film nitride materials MgMoN₂, MgWN₂, MgTa₂N₃, and ScTa₂N₂ and one 3D RS ScMoN₂, including their minimal RS-to-RL annealing temperatures. (d) Calculated thermodynamic density of states and transformation energy barriers from the cation-layered RS to structurally layered RL, indicating that all of them except ScMoN₂ should transition from RS to RL structure.

A schematic representation of the new synthetic pathway on an energy scale in the Mg–Mo–N compositional coordinates is shown in Fig. 5a. The first step of the process is the formation of a high-energy, long-range disordered but short-range ordered RS-MgMoN₂ 3D crystal structure from atomically dispersed Mg, Mo, and N precursors (Fig. 5a). The second step is transformation of this 3D structure into a layered 2D-like RL-MgMoN₂ structure with both short-range and long-range cation order (Fig. 5a). Fig. 5b illustrates the potential energy surface at a fixed MgMoN₂ composition in energy vs. configurational space coordinates. The potential well corresponding to the ground-state layered RL-MgMoN₂ structure is very deep and narrow. However, it is separated by a small 100 meV potential energy barrier from a much wider—and hence much more probable—3D RS-MgMoN₂ well (Fig. 5b) that is slightly higher in energy. This small potential barrier corresponds to the facile RS-RL local transformation pathway identified in Fig. 4.

The synthetic pathway reported here is not limited to thin film synthesis methods; it should also apply to bulk synthesis approaches where intimate atomic intermixing is involved. For example, in the case of MgMoN₂ synthesized in bulk by metathesis reaction, we reported that an intermediate 300 – 450 °C heating step to promote Mg–M–N bond formation, followed by 800 – 900 °C annealing of these intermediates successfully resulted in the layered 2D-like RL-MgMoN₂ structure. In contrast, the direct heating of the precursors to the 800 – 900 °C reaction temperature in a sealed ampule results in formation of a 3D RS structure, likely accompanied by volatilization of Mg-N precursors.⁴⁰ Bulk syntheses of MgMoN₂²⁷ and MgWN₂²³ by conventional one-step route have been also reported, but at much higher temperature (1100 °C) and with residual W or Mo and other impurities, corresponding to other synthesis pathways than shown in Fig. 5b. In the case of ScTa₂N₂ bulk powders, heating to 1546 °C for 200 hours was required to obtain a phase-pure product.¹⁰ These very high temperatures and lengthy reaction times illustrate the advantage of our newly discovered facile transformation pathway to synthesis of layered ternary nitrides in both bulk and film forms.

Extension to other layered materials beyond MgMoN₂

To demonstrate the universality of the synthesis pathway discovered in this work for RL MgMoN₂, we assess if it can be translated to other nitride thin film materials. To this end, we attempted synthesis of five other materials with alternating layers of Mg or Sc in *O_h* coordination and Mo, W, or Ta in *T_p* coordination: MgWN₂,²³ MgTa₂N₃,¹³ MgNb₂N₃, ScTa₂N₂,¹⁰ and ScMoN₂, with details to be reported in future publications. Briefly, each of these crystallizes in a 3D disordered RS structure upon thin film synthesis, yet only MgWN₂, MgTa₂N₃, and ScTa₂N₂ have been reported to have a layered 2D-like crystal structure based on bulk synthesis, and neither MgNb₂N₃ nor ScMoN₂ have been reported in the ICSD. As shown in Fig. 5c, thin films of MgWN₂, MgTa₂N₃, MgMoN₂, and ScTa₂N₂ deposited at ambient temperature and annealed at 800 – 1200 °C crystallize in layered 2D-like structures with cation ordering indicated by characteristic low-angle diffraction peaks, in agreement with reference XRD patterns. On the other hand, ScMoN₂ could not be synthesized in the RL structure (Fig. 5c), and the MgNb₂N₃ synthesis results were inconclusive (Fig. S8).

Fig. 5d shows the structure sampling and kinetic barrier modeling results for six ternary nitrides including MgWN₂, MgTa₂N₃, ScTa₂N₂, MgNb₂N₃, ScTa₂N₃, ScMoN₂, in addition to MgMoN₂. For each of these additional materials, 2,000 structures have been sampled by DFT. Total energy calculations for all prototypical structures from Fig. 1 have been evaluated to test if any of these might have lower energy than RL. For all of them, the most occurring structure-type in the sampling is disordered RS with its frequency of occurrence far exceeding any other structure type (see Fig. S9 for complete TDOS for each of these compounds), and we find a high percentage of atoms participating in the RS layered motifs of the

materials with 1-1-2 stoichiometry (Table S1). For all but one of the investigated nitrides, the RL structure has the lowest energy compared to other prototypes and the structures found by sampling. The calculated barriers for the structural transformation from the ordered RS into the ordered RL phase are all in the 0.08 – 0.11 eV/atom range (Fig. S10), and the differences in the barriers correlate well with the differences in the annealing temperatures needed for the realization of a RL phase (Fig. S11). The only exception is ScMoN₂, for which the RL phase is higher in energy than any of the disordered RS structures from structure sampling, indicating that the transformation to the RL structure is unlikely. This theoretical result can be explained by the *O_h* rather than *T_p* coordination preference of the Mo(III) ion with d³ electronic configuration,⁴¹ consistent with the inability to experimentally realize a RL phase for this ScMoN₂ stoichiometry (Fig. 5c). This ScMoN₂ comparison provides a false negative validation for our theoretical method, suggesting it can be used for prediction of other synthesizable layered 2D-like materials.

The successful synthesis of MgWN₂, MgTa₂N₃, MgMoN₂, and ScTa₂N₂ layered nitride materials in thin film form (Fig.5c) and the theoretical explanation of their realization (Fig.5d), support generality of the transformation pathway described in this paper. These results are also interesting because thermoelectric¹¹ and quantum^{21, 20} properties were predicted for these RL materials by theoretical calculations but have not been measured yet due to prior difficulty in thin film synthesis. The general synthesis pathway demonstrated in this work for layered RL structure may also apply to nitrides with KCoO₂-type structures such as SrTiN₂ and BaZrN₂ (Fig. S12), with two distinct coordination environments that recently attracted renewed attention due to their electronic properties.^{42,43} This pathway may also apply other site-layered ternary nitrides, but likely not to cation-layered single-site wurtzite¹⁶ or rocksalt¹⁷ phases. It would be also interesting to perform similar calculations and experiments for the layered nitride and carbide MAX phases⁸, where only 4 – 6 out of >160 materials have been grown in thin film form.⁷

Conclusions

In summary, we synthesized MgMoN₂ with a layered 2D-like crystal structure from a 3D disordered precursor, and quantified the 3D-to-2D transformation pathway by in-situ measurements and theoretical calculations. As-deposited MgMoN₂ thin films crystallize in a rocksalt (RS) structure with 3D octahedral coordination up to a substrate temperature of 600 °C. At higher substrate temperatures, MgN_x evaporates from the film, making it difficult to deposit MgMoN₂ in the thermodynamically stable layered 2D-like rock-salt (RL) structure by conventional thin film deposition methods. Upon heating to 600 °C, the stoichiometric RS precursors deposited at ambient temperature go through negative thermal expansion. Surprisingly, above 700 °C the ostensibly cation-disordered 3D RS precursor rapidly transforms into a cation-ordered layered 2D-like RL structure. Theoretical structure sampling identifies that 99% of the calculated 3D RS structures have layered -Mg-Mo-Mg-Mo- local structural motifs arranged along (111) crystallographic direction, akin to (001)-stacked layers in the 2D-like RL structure, and it predicts local structural regions with shorter-than-average Mo–Mo distances that would be hidden from conventional diffraction measurements. The resulting peak splitting is observed in experimental thin film grazing incidence PDF measurements, supporting the computational model for the long-range disordered but short-range ordered RS structure. The calculated facile crystallographic transformation from a 3D RS to a layered 2D-like RL structure has a 100 meV/atom energy barrier, experimentally measured using on-chip nanocalorimetry. These favorable comparisons of two independent experimental measurements and theoretical calculations validate the discovered 3D-to-2D transformation pathway as a whole.

In conclusion, we identified a new synthesis route to nitride thin films with layered 2D-like crystal structures, namely a pathway starting from layered short-range ordered but long-range disordered 3D bonded precursors. This discovery means that other nitride materials reported to crystallize in disordered 3D structures (like rocksalt or wurtzite) may have short-range order hidden from XRD measurements that

allows them to transform into the thermodynamically stable layered 2D-like crystal structures upon suitable annealing. We demonstrate the universality of this approach by synthesizing layered 2D-like MgWN_2 , MgTa_2N_3 , and ScTa_2N_2 , which were predicted to have interesting quantum and electronic properties. Moreover, we theoretically explain the experimental observation that these materials could be synthesized in layered 2D-like structures from 3D precursors, whereas ScMoN_2 could not. The 3D-to-2D synthesis pathway described in this paper also implies that the long-range order of the final layered product should be possible to control through altering short-range order of the precursor during the synthesis. This control of cation ordering in the final structure is important for fine-tuning materials with quantum properties like critical temperature that are sensitive to local symmetry, and semiconductor properties like the band gap that can be tuned by cation disorder.

Methods

Experimental

In brief, we synthesized thin films (typically 150 – 300 nm thick) of Mg–Mo–N by radio-frequency (RF) co-sputtering from metallic Mg and Mo precursors in an Ar and N_2 atmosphere onto Si substrates without (80 °C) and with (<600 °C) intentional heating, and subjected them to rapid thermal annealing in flowing N_2 at 600 – 1200 °C for 3 – 30 min. Metal composition was quantified with X-ray fluorescence (XRF), and anion composition was measured with Auger electron spectroscopy (AES). The crystal structure determined from laboratory and synchrotron X-ray diffraction (XRD) was measured as a function of the Mg–Mo–N chemical composition and at various deposition and annealing temperatures. More details about experimental synthesis and characterization are presented next.

Multiple Mg–Mo–N thin film sample libraries with different with Mg/Mo composition gradients were deposited by RF co-sputtering onto ambient-temperature (60 – 80 °C due to unintentional heating) commercial Si substrates, some with a CVD-grown SiN_x layer, from 2" (50 mm) diameter Mg and Mo targets held at 30 – 60 W power. Typical depositions were performed in a mixture of flowing $\text{Ar}/\text{N}_2=6/3$ sccm in a total of 6 mTorr (8×10^{-6} atm) pressure in a vacuum chamber with 10^{-7} Torr (1.3×10^{-9} atm) base pressure for 60 – 120 min, resulting in 150 – 300 nm thin films. Thinner samples deposited for 15 – 30 min on Si/ SiN_x membrane substrates, and thicker samples deposited for 4 – 6 hours on quartz, were deposited for nanocalorimetry and PDF measurements, respectively. Some samples had a 50 nm thin SiN_x or AlN capping layer deposited on the top of the film to prevent surface oxidation during the storage. The synthesized samples have been treated by rapid thermal annealing (RTA, ULVAC MILA-5000 series) in the 600 – 1200 °C temperature range for 3 – 30 min with a 1 min temperature ramp up and a 2 – 5 min temperature quench in flowing N_2 .

Cation composition of the Mg–Mo–N films was measured using XRF (Bruker M4 Tornado) and quantified using XMethods software with a manual conversion from wt % to at %. The anion composition and unintentional oxygen content (if any) was determined from AES measurements using standard sensitivity factors for O and N, with Mg and Mo compositions calibrated to those of the XRF values. Nanocalorimetry measurements were performed on as-deposited Mg–Mo–N films in a N_2 atmosphere, with an average heating rate of roughly 10,000 °C/s. The nanocalorimeter sensor includes a Pt thin film heater deposited over a SiN_x membrane which is suspended over a Si frame. The Pt heater also functions as a temperature sensor based on the temperature coefficient of resistance of Pt through calibration using the melting point of Al. A 10 nm alumina barrier was deposited between the sensor and sample using atomic layer deposition to prevent any potential reaction between sample and SiN_x .

Laboratory XRD patterns were collected with Bruker D8 Discover with Cu K α radiation equipped with a two-dimensional (2D) detector and analyzed using Comblgor software,⁴⁴ with data available in NREL's HTEM DB.⁴⁵ In-situ laboratory XRD measurements were performed on a resistively heated stage in a Kapton dome under flowing N₂. To study the kinetic mechanism nucleation and growth during this phase transformation process, we performed analysis of the time-dependent XRD data using sigmoidal Avrami equation from the Johnson–Mehl–Avrami–Kolmogorov (JMAK) model³⁷:

$$I(t)=1-\exp(-kt^n) \quad (1)$$

where I is the measured XRD intensity, $n=n_n+n_g$ are nucleation and growth components of the Avrami exponent, and k is a constant. This model is commonly used to describe isothermal nucleation of growth kinetics in different areas of materials science, for example polarization domains in ferroelectric materials, most recently nitrides.⁴⁶

High-resolution synchrotron grazing incidence wide-angle X-ray scattering (GIWAXS) measurements were performed at beamline 11-3 at the Stanford Synchrotron Radiation Lightsource (SSRL), SLAC National Accelerator Laboratory. The data were collected with a Rayonix 225 area detector at room temperature using a wavelength of $\lambda = 0.9744 \text{ \AA}$, a 1° or 3° incident angle, a 150 mm sample-to-detector distance, and a spot size of $50 \mu\text{m} \times 150 \mu\text{m}$. The diffraction images were integrated and processed with GSAS-II. Synchrotron pair distribution function (PDF) and diffraction (XRD) measurements were measured on select samples grown on quartz substrates at beamline 11-ID-B at the Advanced Photon Source (APS), Argonne National Laboratory. The data were collected in grazing incidence geometry with a wavelength of 0.1432 \AA . The data were integrated using GSAS-II; PDFs were generated using xPDFsuite with $Q_{\text{max}} = 25 \text{ \AA}^{-1}$; and PDF fitting was performed in PDFgui.⁴⁷ LeBail fits were performed on the XRD data with Topas v6 in s.g.225 ($Fm-3m$). The lattice parameter (a) and sample displacement were refined. Peak shapes were fit with a TCHZ function, with the background fit to a 10-term polynomial.

Theoretical

In brief, the first-principles random structure sampling method entails creating a large number of structures with: (i) random lattice vectors and atomic positions, (ii) fixed stoichiometry (e.g. MgMoN₂), and (iii) a fixed number of atoms ($N=24$). These are subsequently relaxed to the closest local minimum on the PES using density functional theory (DFT), and then grouped into classes of equivalent structures. The number of structures belonging to each class, or its frequency of occurrence in the structure sampling, is then taken as the size of a corresponding local minimum on the PES and used in the statistical mechanics treatment of the results. An initial pathway for the proposed mechanism for the transformation from RS to RL was computed via atom-to-atom mapping.³⁹ The pair distribution function (PDF) $g(r)$ for the theoretical representation of MgMoN₂ is directly calculated in real space.⁴⁸ More details are described next.

The first principles structure sampling, which is used for structure predictions in this work, proceeds according to the following protocol. In the first step, a large number of structures are generated with random lattice parameters ($a,b,c,\alpha,\beta,\gamma$) using the algorithm that ensures cation-anion coordination.³³ A total of 5,000 structure samples are constructed for MgMoN₂, and 2,000 structures for MgWN₂ and the other studied nitride materials. In the second step all random structures are relaxed, including the cell parameters and atomic positions, using density functional theory (DFT) to the closest local minimum, following the steepest descent algorithms as implemented in VASP computer code⁴⁹ within the PAW formalism using soft pseudopotential for N and normal pseudopotentials for all metals. This choice of pseudopotentials balances computational efficiency and structural accuracy. Monkhorst-Pack k -point grid with the subdivision determined by the VASP $R_k=20$ parameter and plane wave cutoff of 340 eV are used. Automatic k -point grid generation with length parameter $R_k=20$ enables consistent k -grid density for the

random sampling, in which structures are initialized with random lattice vectors. Relaxations are considered converged when the forces on atoms are all below 0.01 eV/Å and the final pressure is below 3 kbar.

The relaxed structures are grouped into classes having the same underlying (parent) crystal structure. The classification is performed based on (a) the space group assignment of the equivalent structure in which all of the cations (Mg and Mo in case of MgMoN₂) are labeled the same, and (b) the first shell coordination of the atoms. For the samples grouped into classes with the same underlying structure, partition functions and corresponding configurational free energies are then evaluated as a function of temperature using energy per formula unit in the Boltzmann exponents.³⁵ To analyze the local cation ordering in different predicted disordered RS MgMoN₂ structure variants, each structure was scanned for reproduction of the *M–M* distances and bond angles in the cation-layered RS motif, followed by visual verification of the specific arrangement of diagonal edge-sharing *M*-centered octahedra.

To calculate pair distribution function (PDF) $g(r)$ in real space,⁴⁸ for each of the 314 RS-type structures obtained from the random structure sampling, we compute atom type pair specific PDFs $g_{\alpha\beta}^S(r)$ where α and β denote different atom types. The ensemble averaged $g_{\alpha\beta}(r)$ is then obtained through a sum over each structure S of the ensemble. The total PDF $g(r)$ is then easily obtained as a weighted sum of the partials with the weights coming from an approximation of the X-ray atomic form factors $f_{\alpha}(Q)$. The function mainly used in this work is the reduced PDF $G(r)$ as it can directly be obtained from the Fourier transform of XRD measurements:

$$G(r) = 4\pi r n_0 (g(r) - 1) \quad (2)$$

The partials $G_{\alpha\beta}(r)$ are obtained in a similar way by just replacing $g(r)$ by the appropriate partial $g_{\alpha\beta}(r)$. More details of the PDF calculations are provided in the supplementary materials.

To compute an initial pathway for the proposed mechanism for the transformation from RS to RL, different supercell representations are chosen for the initial and final structures, and combinations of cells with maximum volume overlap are chosen for further analysis.³⁹ For each choice of cells, atoms are matched between the initial and final cell, solving the assignment problem using the Munkres algorithm. We start by modeling a simple transformation as if all cations have the same chemical identity, and then after the mechanism is found we re-label the atoms based on their correspondence between the two structures. In this way, we find a particular ordering in the RS phase that produces the simplest transformation based on our structure mapping. For the ordered structure, the minimum energy pathway at zero kelvin was computed using solid-state nudged elastic band (SSNEB)⁵⁰ and was considered converged when forces between images were reduced to 0.1 eV/Å, and the barriers were estimated using the climbing image method. Evaluation of upper bounds for the barrier for transformation with disorder were performed by performing site swaps between Mg and Mo in 1×1×2, 1×2×1, and 2×1×1 supercells. Energies of images along these pathways are computed without any relaxations, and therefore represent an upper bound of the energy relative to that which would be found using SSNEB. Under cation disorder conditions, the rate-determining step is the inversion of the octahedra rather than the shift of the N atoms, but the barrier associated with this step remains approximately 90 meV/atom or less. When all layers contain 50% Mo and 50% Mg (red line in Fig. S7), some of the site swaps associated with this model increase rather than decrease the energy of the RL structure to above its associated RS structure.

Acknowledgements

This work was authored in part at the National Renewable Energy Laboratory (NREL), operated by Alliance for Sustainable Energy, LLC, for the U.S. Department of Energy (DOE) under Contract No. DE-AC36-08GO28308. Funding was provided by the Office of Science (SC), Basic Energy Sciences (BES), Materials Chemistry program, as a part of the Early Career Award “Kinetic Synthesis of Metastable Nitrides.” (experimental results), with contribution from NSF Career Award No. DMR-1945010 (computational results). Nanocalorimeter fabrication was performed in part at the NIST Center for Nanoscale Science & Technology (CNST). Use of the Stanford Synchrotron Radiation Lightsource, SLAC National Accelerator Laboratory is supported by DOE’s SC, BES under Contract No. DE-AC02-76SF00515. This research used resources of the Advanced Photon Source, a U.S. Department of Energy (DOE) Office of Science user facility operated for the DOE Office of Science by Argonne National Laboratory under Contract No. DE-AC02-06CH11357. R.W.S. acknowledges support from the Director’s Fellowship within NREL’s Laboratory Directed Research and Development program. We would like to thank Craig Perkins for help with AES analysis; Nicholas Strange for assistance with SSRL data collection; Uta Ruett and Moira Miller for assistance with APS data collection; Baptiste Julien and Kei Yazawa for useful discussions. This work used high-performance computing resources located at NREL and sponsored by the Office of Energy Efficiency and Renewable Energy. Certain commercial equipment, instruments, or materials are identified in this document. Such identification does not imply recommendation or endorsement by the National Institute of Standards and Technology (NIST), nor does it imply that the products identified are necessarily the best available for the purpose. The views expressed in the article do not necessarily represent the views of the DOE or the U.S. Government.

Data availability

The data supporting the findings of this study are available within the paper and its Supplementary Information files. Raw data for experimental thin film results can be obtained from the <https://hitem.nrel.gov/> public repository. Other source data will be provided with this paper.

References

1. Fleming, G. R. & Ratner, M. A. Grand challenges in basic energy sciences. *Phys Today* **61**, 28–33 (2008).
2. Kreider, M. E. *et al.* Nitride or Oxynitride? Elucidating the Composition-Activity Relationships in Molybdenum Nitride Electrocatalysts for the Oxygen Reduction Reaction. *Chemistry of Materials* **32**, 2946–2960 (2020).
3. Nakamura, Y. *et al.* Superconducting qubits consisting of epitaxially grown NbN/AlN/NbN Josephson junctions. *Appl Phys Lett* **99**, 212502 (2011).
4. Jiang, K. *et al.* Mechanical cleavage of non-van der Waals structures towards two-dimensional crystals. *Nature Synthesis* **2022 2:1 2**, 58–66 (2022).
5. Zhang, K., Feng, Y., Wang, F., Yang, Z. & Wang, J. Two dimensional hexagonal boron nitride (2D-hBN): Synthesis, properties and applications. *J Mater Chem C Mater* **5**, 11992–12022 (2017).
6. Shur, M., Gelmont, B. & Asif Khan, M. Electron mobility in two-dimensional electron gas in AlGaIn/GaN heterostructures and in bulk GaN. *Journal of Electronic Materials* **1996 25:5 25**, 777–785 (1996).
7. Biswas, A., Natu, V. & Puthirath, A. B. Thin-film growth of MAX phases as functional materials. *Oxford Open Materials Science* **1**, (2020).
8. Lim, K. R. G. *et al.* Fundamentals of MXene synthesis. *Nature Synthesis* **2022 1:8 1**, 601–614 (2022).
9. Yamane, H. & DiSalvo, F. J. Sodium flux synthesis of nitrides. *Progress in Solid State Chemistry* **51**, 27–40 (2018).

10. Niewa, R., Zharebtsov, D. A., Schnelle, W. & Wagner, F. R. Metal-metal bonding in ScTaN₂. A new compound in the system ScN-TaN. *Inorg Chem* **43**, 6188–6194 (2004).
11. Pilemalm, R., Pourvskii, L., Mosyagin, I., Simak, S. & Eklund, P. Thermodynamic Stability, Thermoelectric, Elastic and Electronic Structure Properties of ScMN₂-Type (M = V, Nb, Ta) Phases Studied by ab initio Calculations. *Condensed Matter 2019, Vol. 4, Page 36* **4**, 36 (2019).
12. Brokamp, T. & Jacobs, H. Darstellung und Struktur einiger Gemischtvalenter ternärer Tantalnitride mit Lithium und Magnesium. *J Alloys Compd* **183**, 325–344 (1992).
13. Verrelli, R. *et al.* On the study of Ca and Mg deintercalation from ternary tantalum nitrides. *ACS Omega* **4**, 8943–8952 (2019).
14. Gregory, D. H. *et al.* Layered ternary transition metal nitrides; synthesis, structure and physical properties. *J Alloys Compd* **317–318**, 237–244 (2001).
15. Gregory, D. H. Structural families in nitride chemistry. *Journal of the Chemical Society, Dalton Transactions* **7**, 259–270 (1999).
16. Greenaway, A. L. *et al.* Ternary Nitride Materials: Fundamentals and Emerging Device Applications. <https://doi.org/10.1146/annurev-matsci-080819-012444> **51**, 591–618 (2021).
17. Bauers, S. R. *et al.* Ternary nitride semiconductors in the rocksalt crystal structure. *Proc Natl Acad Sci U S A* **116**, 14829–14834 (2019).
18. Yang, M. *et al.* Anion order in perovskite oxynitrides. *Nature Chemistry* **2010 3:1** **3**, 47–52 (2010).
19. Kageyama, H. *et al.* Expanding frontiers in materials chemistry and physics with multiple anions. *Nature Communications* **2018 9:1** **9**, 1–15 (2018).
20. Huang, H., Jin, K. H. & Liu, F. Alloy Engineering of Topological Semimetal Phase Transition in MgTa₂-xNb_xN₃. *Phys Rev Lett* **120**, 136403 (2018).
21. Wu, Q., Piveteau, C., Song, Z. & Yazyev, O. V. MgTa₂N₃: A reference Dirac semimetal. *Phys Rev B* **98**, 081115 (2018).
22. Bordeenithikasem, P. *et al.* Determination of critical cooling rates in metallic glass forming alloy libraries through laser spike annealing. *Scientific Reports* **2017 7:1** **7**, 1–9 (2017).
23. Rom, C. L. *et al.* Bulk and film synthesis pathways to ternary magnesium tungsten nitrides. *J Mater Chem C Mater* **11**, 11451–11459 (2023).
24. Zakutayev, A., Bauers, S. R. & Lany, S. Experimental Synthesis of Theoretically Predicted Multivalent Ternary Nitride Materials. *Chemistry of Materials* **34**, 1418–1438 (2022).
25. Woods-Robinson, R. *et al.* Role of disorder in the synthesis of metastable zinc zirconium nitrides. *Phys Rev Mater* **6**, 043804 (2022).
26. Arca, E. *et al.* Redox-Mediated Stabilization in Zinc Molybdenum Nitrides. *J Am Chem Soc* **140**, 4293–4301 (2018).
27. R. Verrelli *et al.* On the viability of Mg extraction in MgMoN₂: a combined experimental and theoretical approach. *Physical Chemistry Chemical Physics* **19**, 26435–26441 (2017).
28. Liangbiao Wang *et al.* Solid state synthesis of a new ternary nitride MgMoN₂ nanosheets and micromeshes. *J Mater Chem* **22**, 14559–14564 (2012).
29. Tholander, C., Andersson, C. B. A., Armiento, R., Tasnádi, F. & Alling, B. Strong piezoelectric response in stable TiZnN₂, ZrZnN₂, and HfZnN₂ found by ab initio high-throughput approach. *J Appl Phys* **120**, 225102 (2016).
30. Bem, D. S., Lampe-Önnerud, C. M., Olsen, H. P. & zur Loye, H.-C. Synthesis and Structure of Two New Ternary Nitrides: FeWN₂ and MnMoN₂. *Inorg Chem* **35**, 581–585 (1996).
31. Cao, B., Veith, G. M., Neufeind, J. C., Adzic, R. R. & Khalifah, P. G. Mixed close-packed cobalt molybdenum nitrides as non-noble metal electrocatalysts for the hydrogen evolution reaction. *J Am Chem Soc* **135**, 19186–19192 (2013).
32. Jones, E. B. & Stevanović, V. Polymorphism in elemental silicon: Probabilistic interpretation of the realizability of metastable structures. *Phys Rev B* **96**, 184101 (2017).

33. Stevanović, V. Sampling Polymorphs of Ionic Solids using Random Superlattices. *Phys Rev Lett* **116**, 075503 (2016).
34. Jankousky, M., Garrity, E. M. & Stevanović, V. Polymorphism of group-IV carbides: Structures, (meta)stability, electronic, and transport properties. *Phys Rev Mater* **7**, 053606 (2023).
35. Jones, E. B. & Stevanović, V. The glassy solid as a statistical ensemble of crystalline microstates. *npj Computational Materials* **2020 6:1** **6**, 1–6 (2020).
36. Ndione, P. F. *et al.* Control of the electrical properties in spinel oxides by manipulating the cation disorder. *Adv Funct Mater* **24**, 610–618 (2014).
37. Shirzad, K., Society, C. V.-J. of the R. & 2023, undefined. A critical review on applications of the Avrami equation beyond materials science. *royalsocietypublishing.orgK Shirzad, C VineyJournal of the Royal Society Interface, 2023*•*royalsocietypublishing.org* **20**, (2023).
38. Yi, F. & Lavan, D. A. Nanocalorimetry: Exploring materials faster and smaller. *Appl Phys Rev* **6**, (2019).
39. Stevanović, V. *et al.* Predicting kinetics of polymorphic transformations from structure mapping and coordination analysis. *Phys Rev Mater* **2**, 033802 (2018).
40. Todd, P. K., Fallon, M. J., Neilson, J. R. & Zakutayev, A. Two-Step Solid-State Synthesis of Ternary Nitride Materials. *ACS Mater Lett* **3**, 1677–1683 (2021).
41. Kertesz, M. & Hoffmann, R. Octahedral vs. Trigonal-Prismatic Coordination and Clustering in Transition-Metal Dichalcogenides. *J Am Chem Soc* **106**, 3453–3460 (1984).
42. Shang, K. *et al.* Tolerance Factor and Phase Stability of the KCoO₂-Type AMN₂ Nitrides. *Inorg Chem* **63**, 4168–4175 (2024).
43. Shiraishi, A. *et al.* Design, Synthesis, and Optoelectronic Properties of the High-Purity Phase in Layered AETMN₂ (AE = Sr, Ba; TM = Ti, Zr, Hf) Semiconductors. *Inorg Chem* **61**, 6650–6659 (2022).
44. Talley, K. R. *et al.* COMBIgor: Data-analysis package for combinatorial materials science. *ACS Comb Sci* **21**, 537–547 (2019).
45. Zakutayev, A. *et al.* An open experimental database for exploring inorganic materials. *Sci Data* **5**, 180053 (2018).
46. Yazawa, K. *et al.* Anomalously abrupt switching of wurtzite-structured ferroelectrics: simultaneous non-linear nucleation and growth model. *Mater Horiz* **10**, 2936–2944 (2023).
47. Farrow, C. L. *et al.* PDFfit2 and PDFgui: computer programs for studying nanostructure in crystals. *Journal of Physics: Condensed Matter* **19**, 335219 (2007).
48. Keen, D. A. A comparison of various commonly used correlation functions for describing total scattering. *urn:issn:0021-8898* **34**, 172–177 (2001).
49. Kresse, G. & Joubert, D. From ultrasoft pseudopotentials to the projector augmented-wave method. *Phys Rev B* **59**, 1758 (1999).
50. Sheppard, D., Xiao, P., Chemelewski, W., Johnson, D. D. & Henkelman, G. A generalized solid-state nudged elastic band method. *Journal of Chemical Physics* **136**, 74103 (2012).

Supplementary information for

Synthesis pathways to thin films of stable layered nitrides

Andriy Zakutayev^{1*}, Matthew Jankousky², Laszlo Wolf², Yi Feng³, Christopher L. Rom¹, Sage R. Bauers¹,
Olaf Borkiewicz⁴, David A. LaVan³, Rebecca W. Smaha¹, Vladan Stevanovic²

¹ National Renewable Energy Laboratory

² Colorado School of Mines

³ National Institute of Standards and Technology

⁴ Argonne National Laboratory

*andriy.zakutayev@nrel.gov

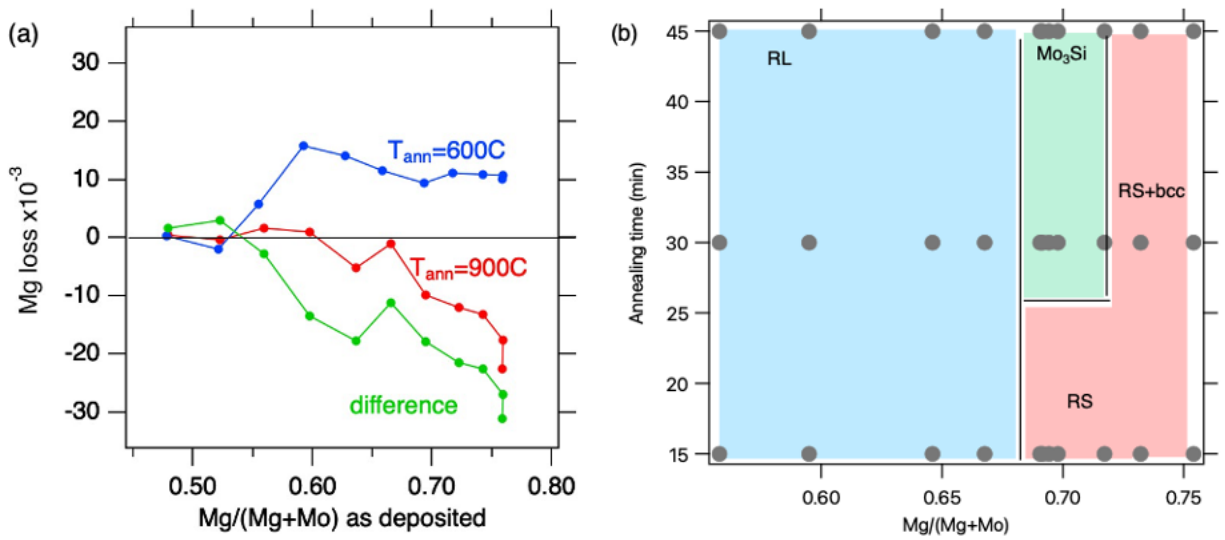


Figure S1: (a) Composition measurements of Mg–Mo–N films as a function of Mg/(Mg+Mo) composition after 600 °C and 900 °C annealing, showing increased Mg loss up to 3% at film compositions that were initially Mg-rich; (b) Time dependence of the phase for Mg–Mo–N films annealed at 1000 °C as a function of time, showing that the material remains in the RL or RS structure until Mo starts reacting with Si substrate forming Mo_3Si .

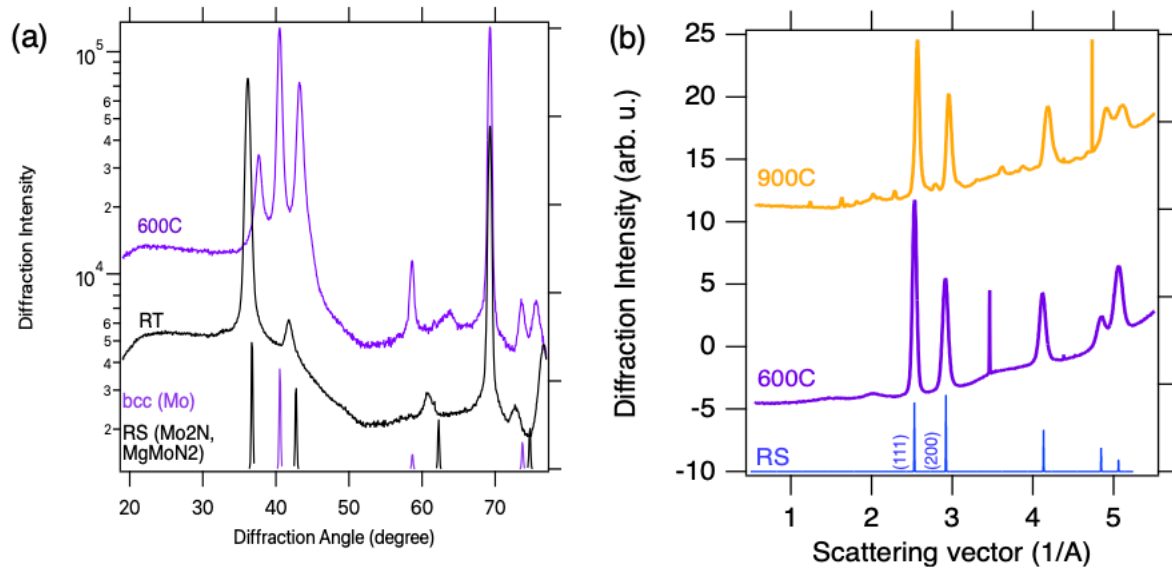


Figure S2: (a) Mg–Mo–N films grow in the RS structure at both ambient (RT) and at 600 – 700 °C substrate temperatures, as measured with laboratory XRD; (b) Synchrotron GIWAXS measurement results for Mg_3MoN_4 annealed at 600 and 900 °C, indicating RS structure as measured at SSRL 11-3.

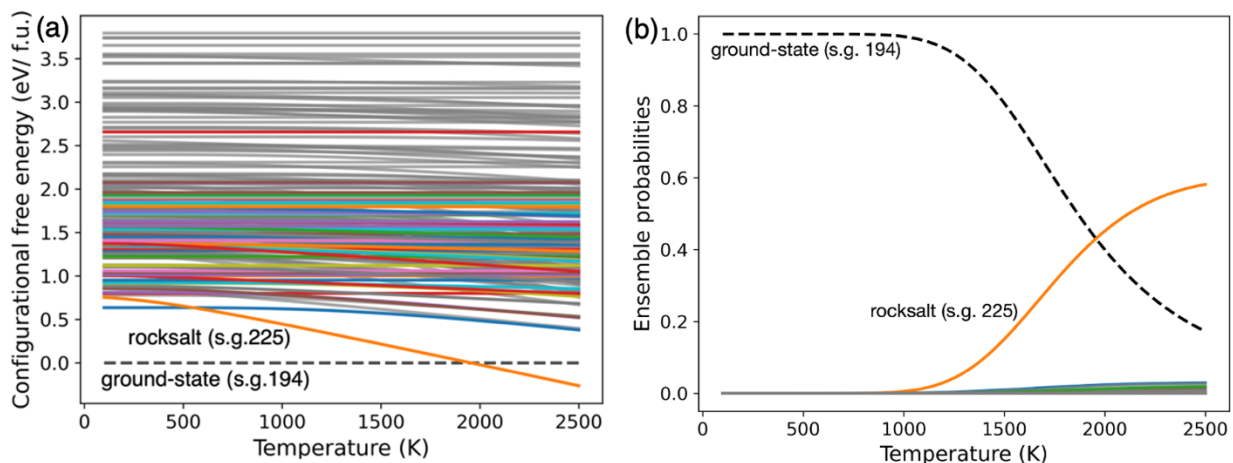


Figure S3: Polymorph sample theoretical results: (a) Configurational free energy as a function of temperature of all structure types of MgMoN_2 computed as described in the Methods section. (b) ensemble probabilities for the two most likely structures in thermodynamic equilibrium, showing that RS polymorph becomes dominant over the ground state RL structure above 2000 K.

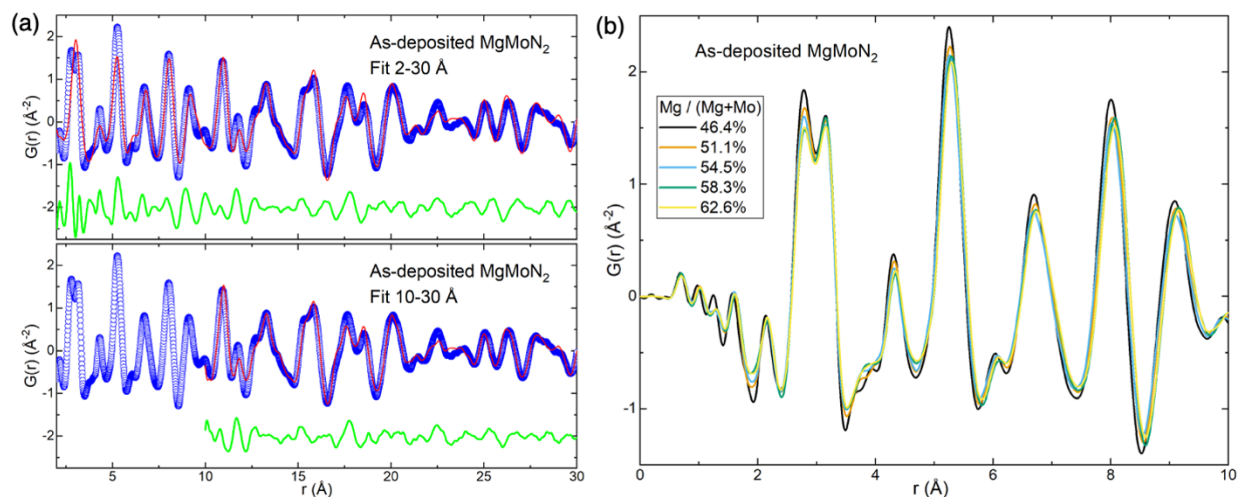


Figure S4: (a) PDF data (blue circles) of as-deposited MgMoN_2 with $\text{Mg}/(\text{Mg}+\text{Mo}) = 51.1\%$ fit with a disordered rocksalt model across the full r -range (2 – 30 Å, top) and a longer-length scale range (10 – 30 Å, bottom). The red line is the fit, and the green line is the difference. (b) PDF data of as-deposited MgMoN_2 with varying cation ratios $\text{Mg}/(\text{Mg}+\text{Mo})$. The data were collected at APS 11-ID-B.

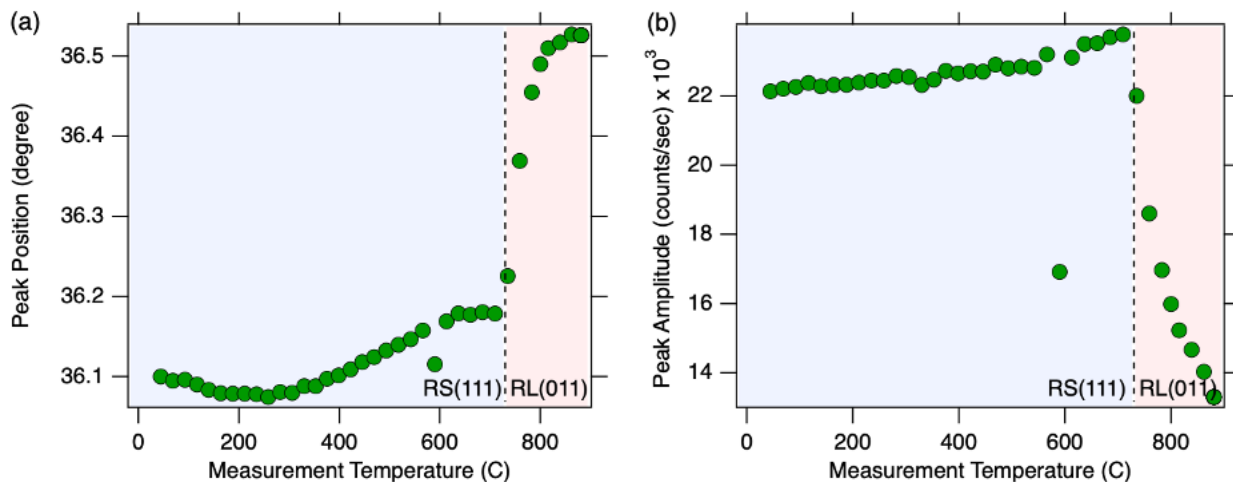


Figure S5: Temperature-dependent laboratory XRD results: (a) positions and (b) and amplitudes of the RS (111) and RL (011) peaks, illustrating apparent increase in decrease in lattice volume of the RS phase above 300 °C indicative of the negative thermal expansion.

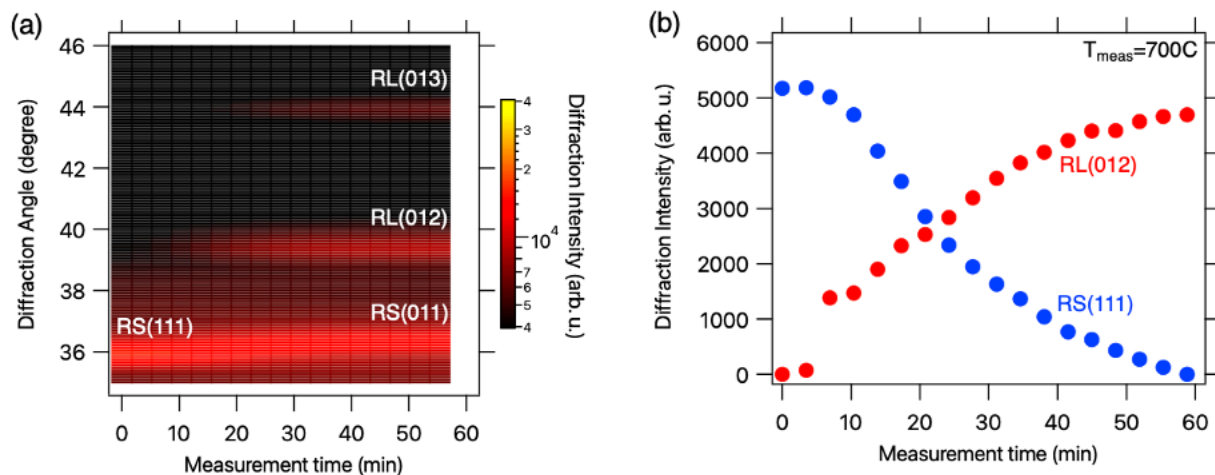


Figure S6: Time-dependent laboratory XRD results: (a) Time-dependent XRD showing evolution of the structure from RS to RL structure at 712 °C; (b) time-dependent XRD peak intensities at 712 °C measurement temperatures showing sigmoidal change described by the KAI model.

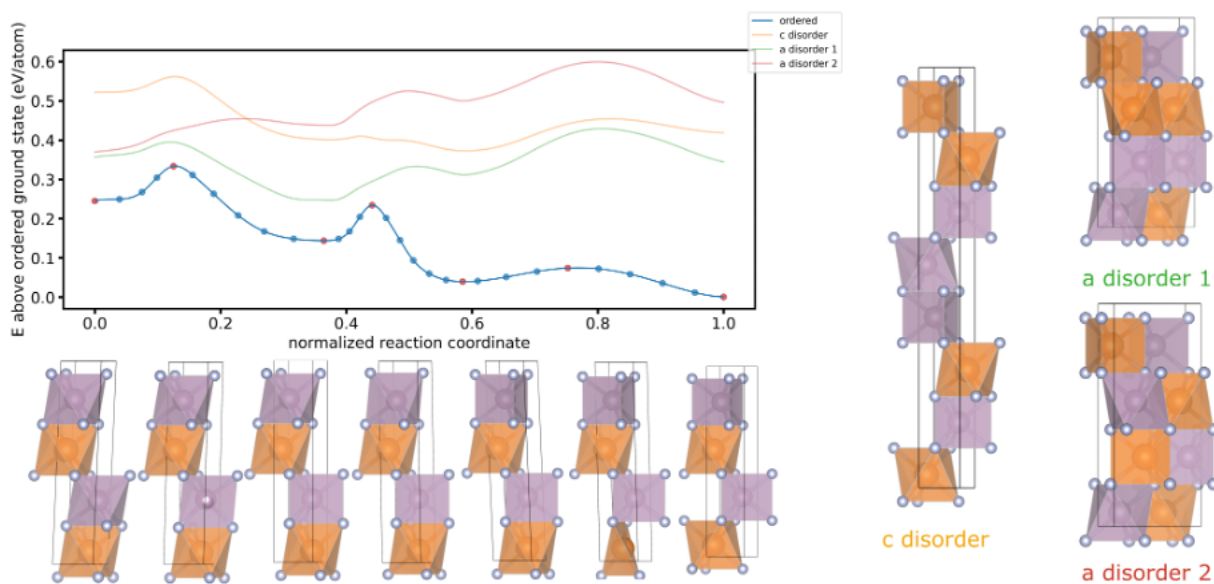


Figure S7: The energy profile for the transformation of the layered RS structure to the RL structure in the presence of three different versions of atomic disorder shown on the right, as compared to an ordered pathways, as calculated using SS-NEB. The structures of local maxima and minima along the ordered pathway are shown below.

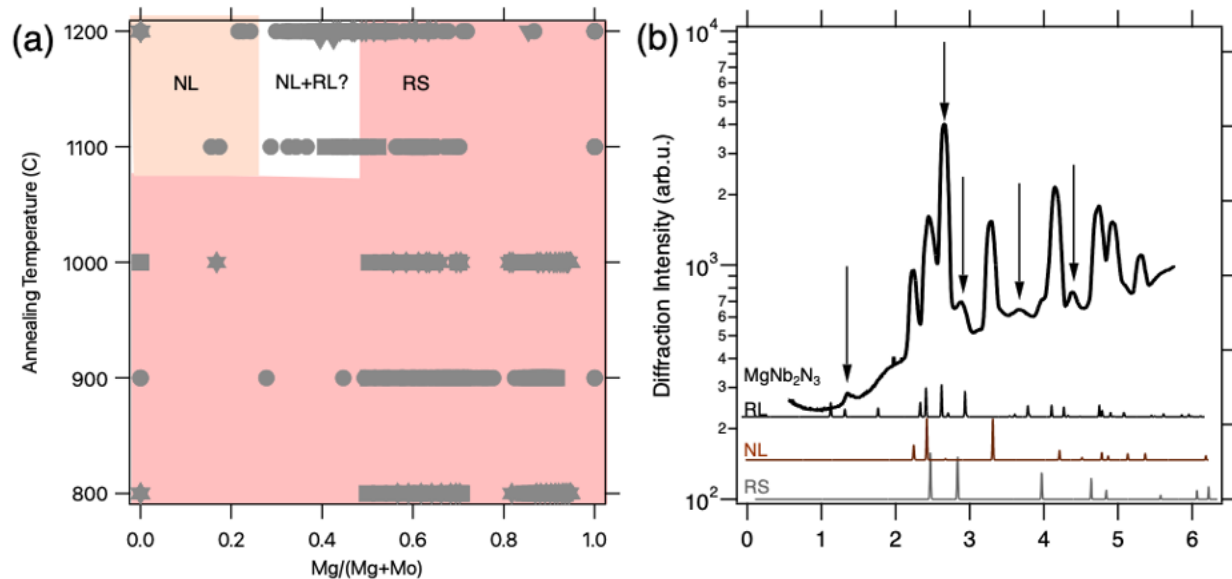
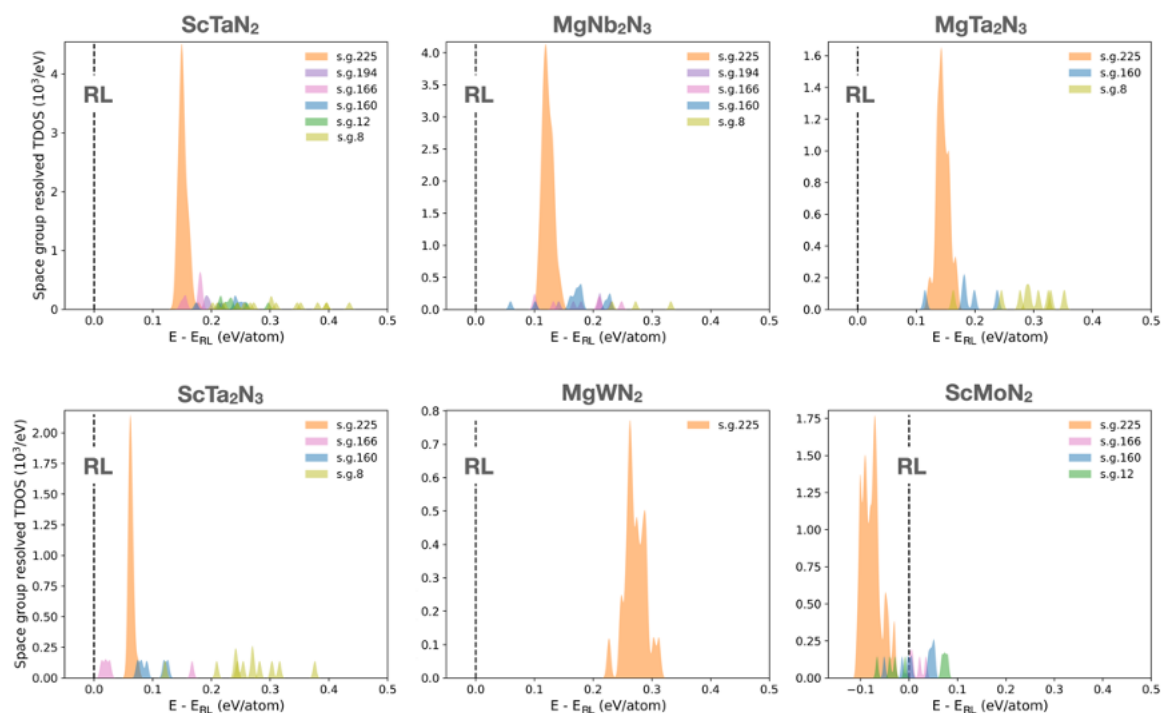


Figure S8: The results of the synthesis attempt for MgNb_2N_3 compound. (a) phase map of annealing results for Mg-Nb-N films, showing strong competition between RS and nickeline (NL) phases, with some minority RL phase in between. (b) A representative XRD pattern from the mixed phase region, showing a minority RL structure peak indicated by arrows, in the dominant nickeline (NL) structure of NbN phase.



Figure

S9: Comparison between calculated TDOS of the disordered RS structure (s.g.225) and other predicted structures for all six calculated nitride compounds, with the energies expressed relative to the RL layered structure type.

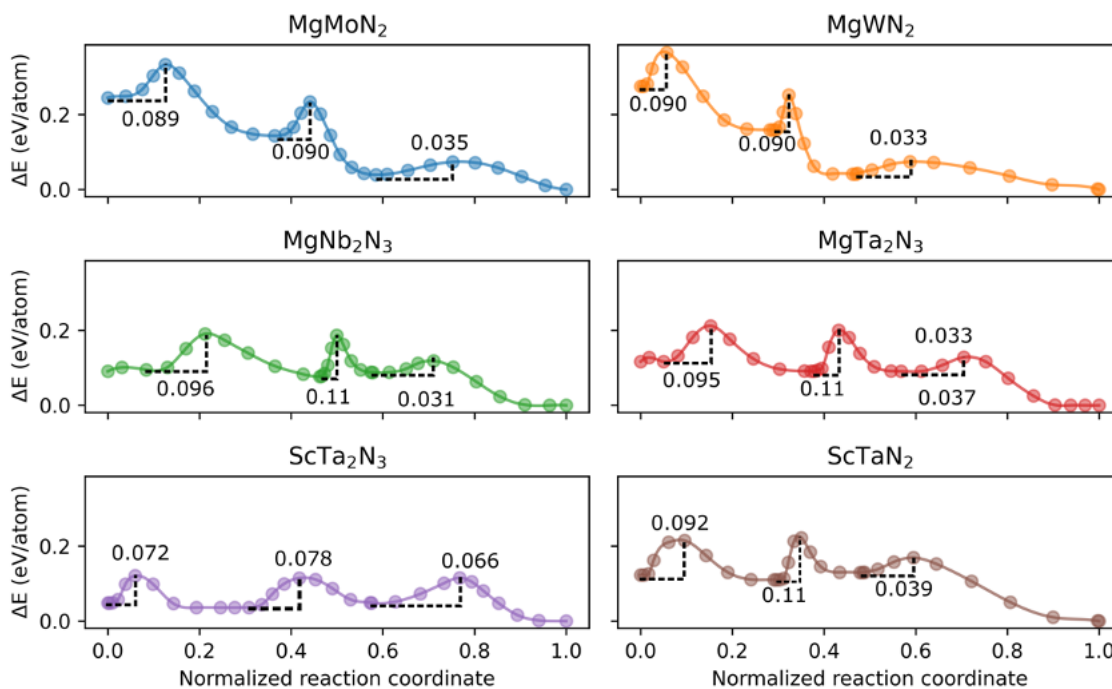


Figure S10: The calculated barriers for the structural transformation from the ordered RS phase into the ordered RL phase for six calculated ternary nitride compounds using solid state NEB method.

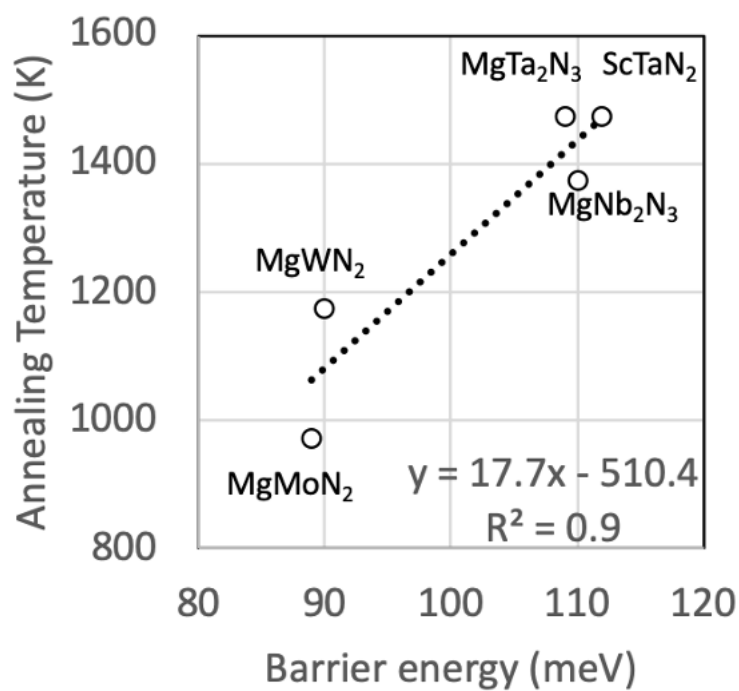


Figure S11: Correlation between the calculated transformation energy barriers and measured minimal annealing temperatures needed for the transformation from RS to RL phase.

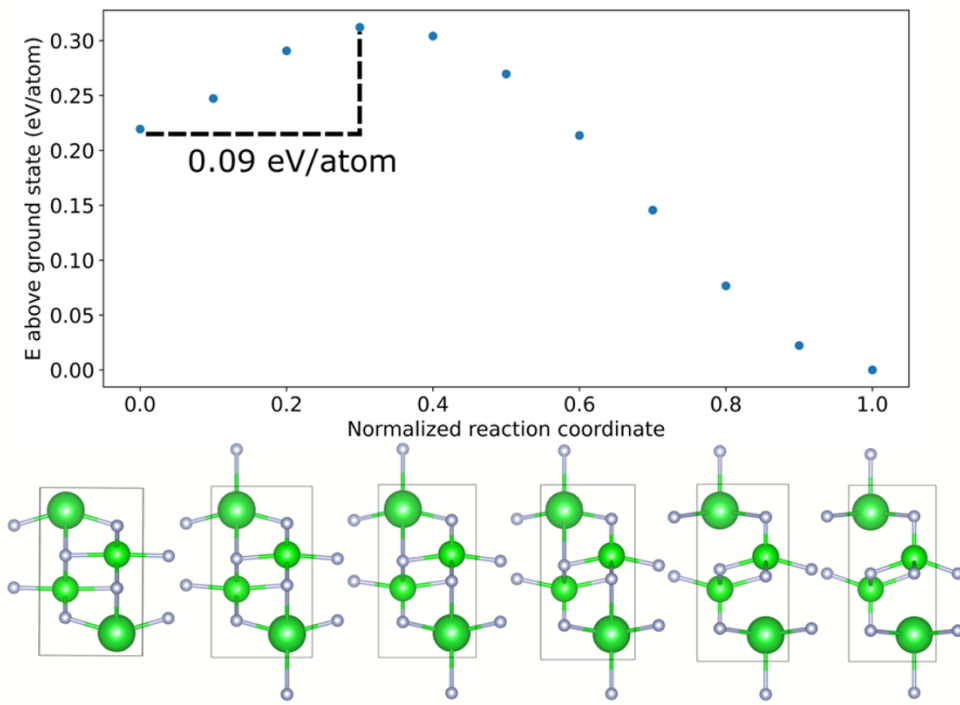


Figure S12: The upper bound of the energy transformation barrier for unrelaxed transformation pathway for BaZrN₂, from cation-ordered rocksalt-derived structure (space group *Pmmn*) to site-ordered KCoO₂-type structure.

Table S1: Number of RS structures identified in structure sampling of ternary nitrides with 1-1-2 stoichiometry, and the fraction of the atoms participating in at least one cation-layered RS motifs. Similar results are also given for a motif along different axes in MgMoN₂.

Composition (direction)	Total Number of Structures from DFT sampling	Number of RS-like structures	RS-like structures with identified layered RS motif	$\left\langle \frac{\text{cations in motif}}{\text{cations in structure}} \right\rangle$
MgMoN ₂	4827	314	314	99.7%
MgMoN ₂ (100/110)	4827	314	314	99.9%
MgMoN ₂ (111)	4827	314	312	88.2%
MgWN ₂	1954	26	26	99.3%
ScMoN ₂	1898	71	71	99.9%
ScTaN ₂	1939	80	80	98.7

PDF calculation methods:

For each of the 314 RS-type structures obtained from the structure sampling, we compute atom type pair specific PDFs $g_{\alpha\beta}^S(r)$ where α and β denote different atom types:⁴⁸

$$g_{\alpha\beta}^S(r) = \left\langle \frac{1}{4\pi r^2 n_0 c_\beta} \frac{dN_{\alpha\beta}(r)}{dr} \right\rangle_\alpha$$

Here n_0 is the global concentration of atoms (number of atoms/volume), c_β is the atomic fraction of β atoms. $dN_{\alpha\beta}(r)$ represents the number of β atoms in a spherical region of thickness dr at the distance r from a particular α atom, the angle brackets $\langle \dots \rangle_\alpha$ denotes an average over all α atoms of the structure.

The ensemble averaged $g_{\alpha\beta}(r)$ is then obtained through a sum over each structure S of the ensemble:

$$g_{\alpha\beta}(r) = \sum_S g_{\alpha\beta}^S(r) P^S \frac{n^S}{\langle n \rangle}$$

Where P^S is the ensemble probability of structure S which is taken to be $\frac{1}{\text{number of structures}}$ we are working in the high temperature limit. n^S is the atom concentration of structure S while $\langle n \rangle$ is the average atom concentration over the ensemble.

The total PDF $g(r)$ is then easily obtained as a weighted sum of the partials with the weights coming from an approximation of the X-ray atomic form factors $f_\alpha(Q)$:

$$g(r) = \sum_{\alpha,\beta} \frac{c_\alpha c_\beta Z_\alpha Z_\beta}{\langle Z \rangle} g_{\alpha\beta}(r)$$

Where Z_α is the atomic number of the α atom and $\langle Z \rangle$ is the average atomic number of the system.

We note the greater sharpness of the theoretical PDF comes from the lack of vibrational and/or instrument broadening. The only broadening of the theoretical peaks arises from the diversity of the cation decorations over the RS structure produced by the structure sampling. A slight disagreement in intensity between the experimental and theoretical PDFs for certain peaks is attributed to the metal-nitrogen ($M-N$) coordination shells. This difference is likely due to a combination of slight N deficiency and the complicated grazing incidence geometry in which the experimental data were collected.